

Silicon-Germanium Solid Solutions with Balanced Ionic/Electronic Conductivity for High-Rate All-Solid-State Batteries

Yaru Li, Shengjie Xia, Guantai Hu, Haosheng Li, Yong Qian, Hongmin Zhou, Changhong Wang, and Ning Lin**

Silicon (Si) is a promising anode for all-solid-state batteries (ASSBs) due to its high capacity, but it suffers from low initial Coulombic efficiency (ICE) and poor rate performance. Here, a series of Si–Ge solid solution anodes is synthesized via high-energy ball milling. Incorporating isomorphous Ge, which has a lower band gap and larger atomic radius, enhances electronic conductivity and induces lattice distortion to broaden Li^+ diffusion pathways. The optimized Si_xGe anode achieves balanced electron/ion conductivities (3.4×10^{-5} / 2.34×10^{-5} S cm⁻¹), which are markedly superior to those of pure Si (8.1×10^{-8} / 3.13×10^{-6} S cm⁻¹). This dual enhancement enables efficient lithiation/delithiation and stable interfacial contact. As a result, the Si₇Ge anode delivers a high ICE of 89.4%, a reversible capacity of 2631 mAh g⁻¹, and favorable rate performance (2024 mAh g⁻¹ at 3 C). In full cells with a LiCoO₂ cathode, an ICE of 88.0% and 100 mAh g⁻¹ at 2 C are achieved. An all-solid-state pouch cell with the Si_xGe anode demonstrates stable cycling over 100 cycles at 0.33 C, highlighting its potential for practical ASSBs applications. This work offers a promising route to overcome Si anode limitations through rational alloy engineering.

1. Introduction

With the surging demand for safer, high-energy-density rechargeable batteries, all-solid-state batteries (ASSBs) employing non-flammable inorganic solid electrolytes (SEs) are emerging as a promising next-generation energy storage technology.^[1–3] Achieving high energy density in ASSBs hinges on the development of advanced electrode materials with both high capacity and robust performance.^[4–6] Among candidate anode materials, silicon (Si) stands out due to its high theoretical capacity (3580 mAh g⁻¹ for $\text{Li}_{15}\text{Si}_4$), low voltage plateau (≈ 0.4 V vs. Li^+/Li), natural abundance, and good air stability.^[7–11] However, the inherently low electronic and ionic conductivities of Si severely limit its Li-ion transport kinetics, leading to poor initial Coulombic efficiency (ICE) and unsatisfactory rate performance.^[12–16]

In addition, the large volume expansion of Si during (de)lithiation induces electrode cracking, which disrupts the electronic and ionic transport pathways and compromises the cycling stability.^[17]

To enhance the electronic and ionic conductivities of Si-based anodes for ASSBs, various strategies have been explored, including the development of composite electrode systems, pre-lithiation of Si anodes, and the design of advanced electrode architectures.^[18–21] For instance, Si-SE-C composite anode system is constructed to achieve a high capacity of 2917 mAh g⁻¹ with an improved ICE of 88.7%.^[17] However, the uneven ion and electron transport properties at the heterogeneous Si-SE and SE-C interfaces can induce SE decomposition, ultimately leading to performance degradation over time.^[22–25] Prelithiation of Si has been demonstrated to effectively enhance both electronic and ionic conductivities.^[26] Li-Si alloys synthesized via cold pressing, high-temperature melting, and ball milling have shown significantly improved rate performance and cycling stability, highlighting their potential for high-performance ASSBs.^[27–30] Nevertheless, excessively lithiated Si anodes exhibit limited capacity and reduced ionic conductivity, which increases the risk of lithium plating and short-circuiting, thereby posing serious safety concerns.^[31] Rational electrode architecture

Y. Li, H. Li, Y. Qian, N. Lin
Yongjiang Laboratory
Ningbo, Zhejiang 315201, P. R. China
E-mail: ningl@mail.ustc.edu.cn, ning-lin@ylab.ac.cn

S. Xia, G. Hu, C. Wang
Eastern Institute for Advanced Study
Ningbo Institute of Digital Twin
Eastern Institute of Technology
Ningbo 315200, P. R. China
E-mail: cwang@eitech.edu.cn

S. Xia, G. Hu, C. Wang
Zhejiang Key Laboratory of All-Solid-State Battery
Ningbo Key Laboratory of All-Solid-State Battery
Ningbo 315200, P. R. China

S. Xia
School of Chemistry and Chemical Engineering
Shanghai Jiao Tong University
Shanghai 200240, P. R. China

H. Zhou
Instruments Center for Physical Science
University of Science and Technology of China
Hefei, Anhui 230026, P. R. China

 The ORCID identification number(s) for the author(s) of this article can be found under <https://doi.org/10.1002/aenm.202503265>

DOI: 10.1002/aenm.202503265

design provides another pathway to facilitate charge transport within the electrode. For example, incorporating hard carbon into Li-Si alloy anodes can enhance ionic conductivities, suppress lithium dendrite formation.^[31] Additionally, an Ag@PAP composite binder with dual Li⁺ and electronic conductivity improves the ICE (87.5%) and rate performance ($\approx 2000 \text{ mAh g}^{-1}$ at 2 C).^[32] These comprehensive investigations reveal that limited electronic conductivity impairs electrode kinetics and causes trapped active Li, while poor ionic conductivity accelerates dendrite growth and SE decomposition, highlighting the critical need for balanced transport properties in Si-based anodes. Therefore, the simultaneous enhancement of electronic and ionic transport in Si anodes is critical for the development of high-performance ASSBs. However, precise design and regulation of the ionic and electronic conductivities for Si-based anodes in ASSBs still remain a significant challenge and are yet to be fully explored.

In this work, the incorporation of Ge into Si by the high-energy ball milling process as an anode for ASSBs enables simultaneous enhancement of electronic and ionic conductivities, revealing the critical role of balanced charge transport in achieving high-rate performance of Si-based anodes for ASSBs. The isomorphic Ge component, featuring a lower band gap and larger atomic radius, endows the solid solution anode with higher electronic and ionic conductivity than that of Si. The electronic and ionic conductivities of Si-based anodes can be precisely modulated through controlled incorporation of Ge into the solid solution. Electrochemical measurements combined with systematic qualitative and quantitative analyses reveal that insufficient electronic transport leads to trapped active lithium within the anode, limiting capacity utilization, while inadequate ionic transport promotes Li plating and the formation of unstable SEI. The optimized Si₇Ge anode with well-balanced electronic and ionic transport delivers significantly enhanced electrochemical performance. It delivers a high ICE of 89.4% with a reversible capacity of 2631 mAh g⁻¹, and high rate performance with a capacity of 2024 mAh g⁻¹ at 3 C, significantly outperforming pure Si (425 mAh g⁻¹). In full cells, the Si₇Ge anode paired with a high-voltage LiCO₂ (HV-LCO) cathode achieves an ICE of 88.0% and a discharge capacity of 100 mAh g⁻¹ at 2 C. Furthermore, an all-solid-state pouch cell of Si₇Ge anode and LiNi_{0.88}Co_{0.09}Mn_{0.03}O₂ (NCM) cathode demonstrates stable cycling over 100 cycles at 0.33 C. Our work presents a compelling strategy to address the intrinsic limitations of Si anodes, unlocking high energy density and long-term cycling stability for next-generation ASSBs.

2. Results and Discussion

Tailored Si-Ge solid solutions with controlled stoichiometric ratios were synthesized through high-energy ball milling of nano-sized Si (Figure S1, Supporting Information) and micro-sized Ge powders (Figure S2a,b, Supporting Information). Figure 1a shows the XRD patterns of Si-Ge solid solutions (Si₁₅Ge, Si₇Ge, and Si₃Ge). The characteristic (111) diffraction peak of pristine Si at 28.5° shifts to lower degrees (28.4°, 28.3°, and 28.1°) upon Ge incorporation, indicating the lattice expansion. The absence of Ge diffraction peaks further corroborates the formation of Si-Ge solid solutions. Raman spectroscopy (Figure 1b) reveals a redshift in the Si-Si vibrational mode, further confirming the lattice distortion upon Ge alloying. Figure 1c shows the

SEM images of the Si₇Ge solid solution, which consists of irregular nanoparticles. Accordingly, the micron-sized Ge powder is reduced to nanoparticles after the high-energy ball milling process (Figure S2c,d, Supporting Information). The Si₁₅Ge and Si₃Ge present a similar structure (Figure S3a,b, Supporting Information). Large-area SEM energy dispersive spectroscopy (EDS) analysis of Si₇Ge (Figure S4, Supporting Information) reveals microscale compositional homogeneity. The transmission electron microscopy (TEM) and corresponding EDS mapping images (Figure 1d,e) further confirm the uniform distribution of Si and Ge elements within nanoparticles. The high-resolution TEM image reveals an expanded (111) interplanar spacing of 0.319 nm (Figure 1f) of the Si₇Ge crystal, which is larger than that of pure Si (0.314 nm, Figure S5, Supporting Information), directly indicating Ge-induced lattice expansion at the atomic scale.

The electronic and ionic conductivities of these Si-Ge solid solutions are systematically investigated. As illustrated in Figure 1g, the electronic conductivity is measured using direct current (DC) polarization in a model cell configuration. When a constant DC polarization is applied to the device, the current attributed to the electron contribution after equilibrium is reached (Figure S6, Supporting Information), the slope of the voltage-current relationship represents the electronic resistance of the anode. The electronic conductivities of Si, Si₁₅Ge, Si₇Ge, Si₃Ge, and Ge are calculated as 8.1×10^{-8} , 3.7×10^{-7} , 3.4×10^{-5} , 2.1×10^{-4} , and 0.11 S cm^{-1} , respectively, demonstrating the positive correlation to Ge content.

To evaluate the ionic conductivity of Si-Ge solid solutions, an electron-blocking symmetric cell (SS|Li|LPSCl|Anode|LPSCl|Li|SS) is assembled, and ion transport resistance is measured using electrochemical impedance spectroscopy (EIS), as shown in Figure 1h^[25]. The details of the Li-ion transport resistances and effective ionic conductivity are listed in Table S1 (Supporting Information). The ionic conductivities of Si, Si₁₅Ge, Si₇Ge, Si₃Ge, and Ge are 3.13×10^{-6} , 1.34×10^{-5} , 2.34×10^{-5} , 7.19×10^{-6} , and $3.17 \times 10^{-6} \text{ S cm}^{-1}$, respectively. Figure 1i depicts the variation tendency of electron and Li⁺ conductivity in Si, Si₁₅Ge, Si₇Ge, Si₃Ge, and Ge (Table S2, Supporting Information). The as-synthesized Si₁₅Ge, Si₇Ge, and Si₃Ge demonstrate superior Li⁺ conductivity compared to pure Si and Ge anodes, among which Si₇Ge exhibits the highest ionic conductivity. This variation trend arises from Ge-induced modulation of the lattice structure: moderate Ge could expand the Si lattice, reducing the Li⁺ diffusion barrier; while excessive Ge narrows the diffusion pathways, thereby impeding ion transport^[14].

The electrochemical performance of these as-prepared anode materials was initially evaluated in half-cells with Li-In as the counter electrode. Figure 2a presents the galvanostatic charge-discharge profiles of the Si, Si₁₅Ge, Si₇Ge, Si₃Ge, and Ge anodes. The Si₇Ge anode delivers a high initial delithiation capacity of 2631 mAh g⁻¹ with an enhanced ICE of 89.4%, higher than the pure Si anode (2455 mAh g⁻¹, ICE = 79.2%) and Ge anode (1055 mAh g⁻¹, ICE = 76.6%). The corresponding dQ/dV curves (Figure S7, Supporting Information) show that the Si₇Ge anode exhibits a lower polarization voltage of 0.24 V, compared to 0.32 V for pure Si. As shown in Figure 2b, Si₇Ge anode exhibits improved cycling stability, with a capacity retention of 94.6% after 100 cycles at 0.5 C. Figure 2c reveals that the Si₇Ge anode

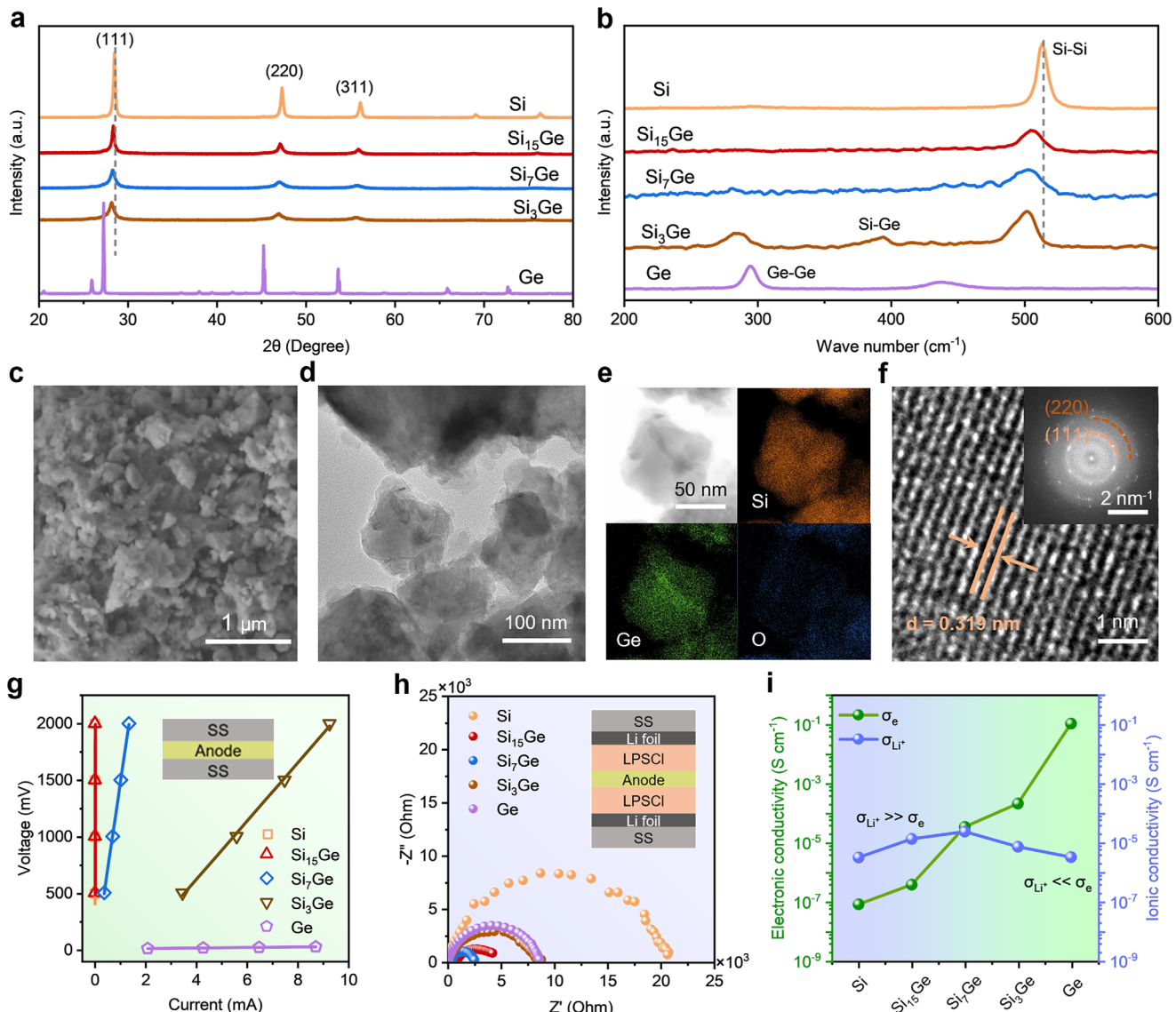


Figure 1. Synthesis and characterization of the silicon-germanium solid solution. a) XRD patterns of pristine Si, Ge, synthesized Si₁₅Ge, Si₇Ge, and Si₃Ge. b) Raman spectra of pristine Si, Ge, synthesized Si₁₅Ge, Si₇Ge, and Si₃Ge. c) SEM image of Si₇Ge. d) TEM image of Si₇Ge. e) Corresponding EDS mapping of Si₇Ge particles. f) High-resolution TEM image with corresponding SAED of Si₇Ge particles. g) Electronic DC polarization measurements of Si, Si₁₅Ge, Si₇Ge, Si₃Ge, and Ge. h) Nyquist plot of the electron-blocking cell in the SS|Li|LPSCl||Anode|LPSCl||Li|SS configuration for various anodes, measured over a frequency range of 7 MHz to 1 Hz. i) Ionic and electronic conductivity results for various anode samples.

outperforms its counterparts in ICE and cycling stability. As shown in Figure 2d, the Si₇Ge anode delivers reversible capacities of 2422, 2369, 2288, 2210, 2142, 2083, and 2024 mAh g⁻¹ at different rates of 0.2 C, 0.5 C, 1 C, 1.5 C, 2 C, 2.5 C, and 3 C, respectively. The Si₇Ge anode achieves the highest capacity retention of 83.8% at 3C, which is far better than that of the Si₁₅Ge (42.0%), Si₃Ge (56.8%), pure Si (18.9%), and Ge (18.2%), as shown in Figure 2e. Statistical consistency of the electrochemical performance was confirmed by testing three independently fabricated cells (Figure S8, Supporting Information). Besides, the Si₇Ge anode exhibits the minimal polarization during the charge-discharge process even at high C-rates (Figure 2f), highlighting the crucial role of the balanced electronic and ionic

conductivity in enhancing electrode kinetics (Figure S9, Supporting Information). To evaluate practical applicability, high-loading ($\approx 2 \text{ mg cm}^{-2}$) anodes were tested under varying external pressures. At 150 MPa and 0.5 C, the Si₇Ge anode delivered a high specific capacity of 2225 mAh g⁻¹ with an areal capacity of 4.8 mAh cm⁻², significantly outperforming the pure Si anode in both capacity and cycling stability. Even under a reduced pressure of 20 MPa, the Si₇Ge anode maintained a higher capacity of 1927 mAh g⁻¹ compared to 1601 mAh g⁻¹ for Si, while retaining superior cycling performance (Figure S10, Supporting Information).

The galvanostatic intermittent titration technique (GITT) was further employed to investigate the Li⁺ diffusion kinetics. As

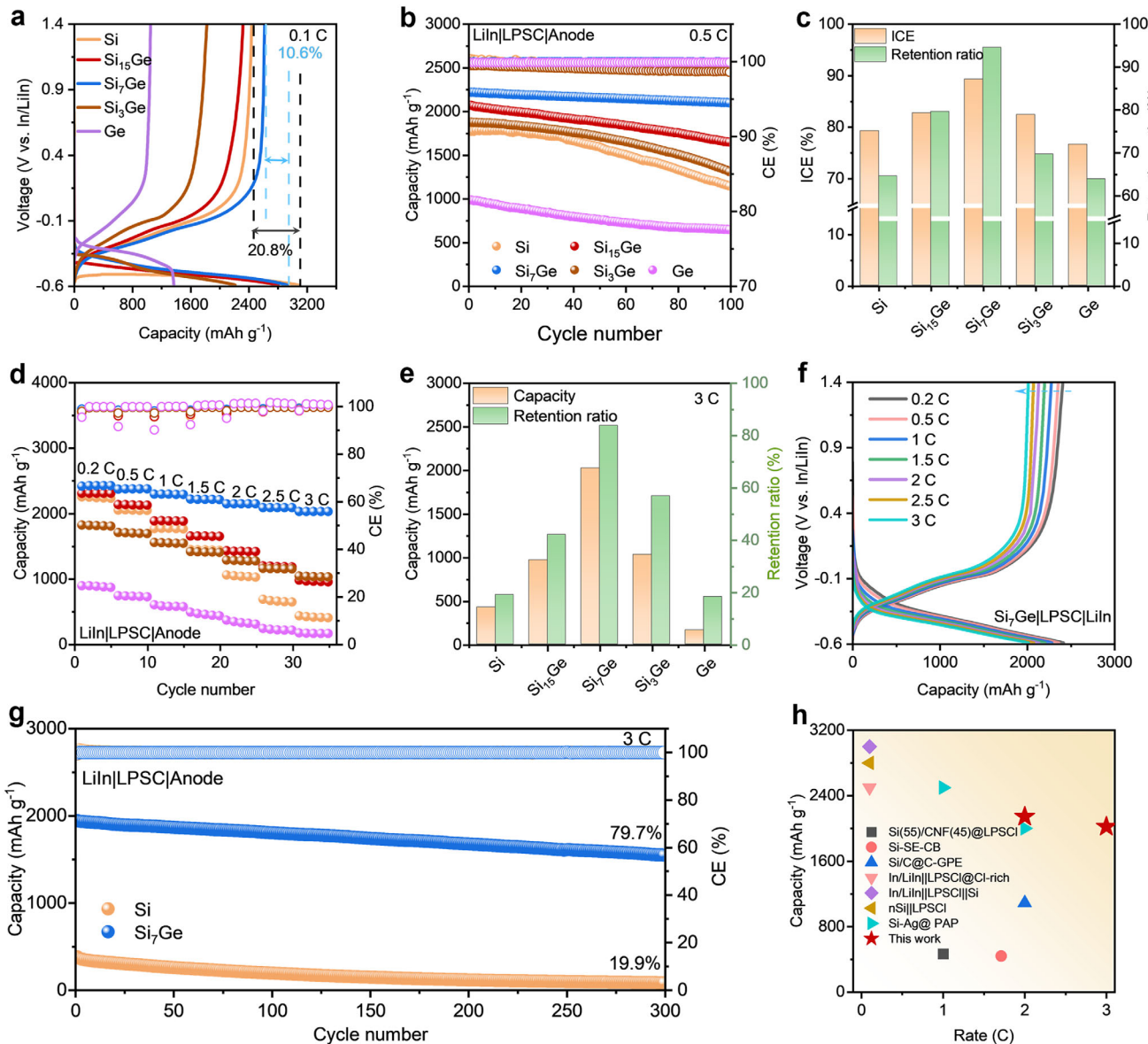


Figure 2. Half-cell electrochemical performance of Si-Ge solid solution anodes in ASSBs. a) Galvanostatic charge and discharge profiles of various anodes during the first cycle at 0.1 C. b) Long-term cycling performance of various anodes at 0.5 C. c) ICE and capacity retention ratio after 100 cycles at 0.5 C for various anodes. d) Rate performance of half-cells with various anodes. e) Capacity and corresponding retention ratio of various anodes at 3 C. f) Galvanostatic charge and discharge profiles of the Si₇Ge anode at different rates. g) Long-term cycling performance of Si and Si₇Ge anodes at 3 C. h) Comprehensive performance statistics for the rate performance of Si-based anodes in ASSBs.

shown in Figure S11a (Supporting Information), GITT profiles of Si, Si₁₅Ge, Si₇Ge, Si₃Ge, and Ge anodes were recorded in half-cells within the voltage range of -0.6 V to 2.0 V. The Li⁺ diffusion coefficients (D_{Li^+}) during the lithiation/delithiation processes for these anodes are presented in Figures S11b,c (Supporting Information), respectively. During lithiation, the D_{Li^+} initially decreases and then gradually increases. Notably, the Si₇Ge anode consistently exhibits the highest D_{Li^+} , with an average value of $4.51 \times 10^{-12} \text{ cm}^2 \text{ s}^{-1}$, which is 2.4 times higher than that of pure Si ($1.85 \times 10^{-12} \text{ cm}^2 \text{ s}^{-1}$). This significant enhancement in ionic transport is attributed to the reduced Li⁺ diffusion barrier caused by Ge-induced lattice expansion. Even during deep delithiation

stages, the Si₇Ge anode maintains superior diffusivity compared to other counterparts.

Figure 2g shows the high-rate (3 C) cycling stability of different electrodes. The Si₇Ge anode maintains a high capacity of 154 mAh g⁻¹ even after 300 cycles (Figure S12, Supporting Information), demonstrating unprecedented high-rate cyclability for Si-based anode in ASSBs. In contrast, the Si anode undergoes rapid capacity degradation, with capacity dropping from 372 to 74 mAh g⁻¹. EIS analysis (Figure S13, Supporting Information) reveals that Ge doping significantly reduces both the bulk and interfacial resistances of the Si₇Ge anode, and enables stable interfacial charge transfer upon cycling. Figure 2h compares the

capacity and rate performance of Si-based anodes in state-of-the-art ASSBs, where the Si_7Ge anode presents superior capacities at high rates, establishing a new benchmark for high-rate Si-based anodes in ASSBs.

The structural and interfacial evolution of the anode electrodes was detected by SEM after 100 cycles. As shown in Figure 3a, the cycled Si anode suffers from substantial volume fluctuations, resulting in electrochemical sintering and the formation of numerous vertically oriented cracks (Figure S14, Supporting Information). Thus, the lateral electron and ion transport within the electrode is severely impeded. The corresponding SEM-EDS mapping images (Figures S15, S16, Supporting Information) reveal substantial presence of P, S, and Cl elements on the anode surface, which is generally originates from residual LPSCl and reaction by-products between the solid-state electrolyte and Si anode during cycling. For the Ge anode (Figure 3b), the surface morphology after cycling is rough and porous, which are attributed to side reactions induced by potential Li plating. Cross-sectional SEM and the EDS mapping images indicate that the Ge anode undergoes electrochemical sintering (Figure S17, Supporting Information), with more side reactions occurring at the interphase (Figures S18–S20, Supporting Information). In contrast, the cycled Si_7Ge anode (Figure 3c) exhibits a smoother surface and a denser cross-section with fewer cracks (Figure S21, Supporting Information), even though a similar electrochemical-sintering phenomenon occurs. Noted, a thin, uniform interphase layer on the anode surface is formed (Figure S22, Supporting Information), suggesting enhanced interfacial compatibility between Si_7Ge and solid electrolytes. The interfacial compatibility between Si_7Ge and the sulfide electrolyte is further demonstrated in subsequent experiments by lower interfacial resistance and fewer decomposition products after cycling. As shown in Figure S23 (Supporting Information), the cycled Si_7Ge anode exhibits a highly uniform distribution of Si and Ge elements, that is, the Si_7Ge alloy structure remains well preserved after cycling. In addition, ex situ SEM observations revealed that the Si_7Ge anode undergoes a lower degree of volume expansion ($\approx 141\%$) compared to the pure Si anode ($\approx 175\%$), accompanied by electrochemical sintering (Figure S24, Supporting Information), which effectively alleviates electrode cracking caused by severe volume fluctuations during cycling (Figure S25, Supporting Information).

To quantitatively elucidate the active Li loss mechanism of the Si anode in ASSBs, a galvanostatic and constant-voltage two-step charging process, combined with chemical titration and gas chromatography analyses, was carried out. Here, Li^+ extraction from the constant-current (CC) step is defined as reversible active Li (RA-Li), Li^+ extraction from the constant-voltage (CV) step is defined as quasi-reversible active Li (QA-Li), and the remaining portion is defined as inactive Li (I-Li). In a liquid-electrolyte system, ‘dead Li’ is generally attributed to the loss of electrical contact^[33]. As a contrast, solid-state systems could maintain robust electrode interfaces under stack pressure, the insufficient Li stripping is primarily produced from kinetic limitations rather than permanent electronic isolation. Notably, the residual active Li can be fully extracted by applying an extended constant-voltage (CV) step^[34]. Thus, in the ASSBs system, RA-Li reflects the intrinsic reversibility of Li intercalation/extraction, while I-Li represents the extent of side reactions between the anode and the LPSCl electrolyte. Figure 3d shows the discharge/charge volt-

age profile ranging from -0.6 V to 1.4 V, with a discharge rate of 0.1 C, followed by CC charging to 1.4 V at 0.1 C and an extended CV charging step at 1.4 V for 16 h. After cycling, the electrode was retrieved from the disassembled cell, sealed in vials, and reacted with ethanol to quantify hydrogen evolution via gas chromatography (Figure 3e). After the CV step, residual active Li is nearly all extracted, as confirmed by quantitative analysis (Table S4, Supporting Information). Figure 3f presents a statistical analysis of RA-Li, QA-Li, and I-Li distributions across various anode systems. Notably, the Si anode exhibits 10.8% QA-Li and 12.0% I-Li, whereas the Ge anode shows 8.2% QA-Li and 13.8% I-Li. These results suggest that the reversible capacity of the Si anode is primarily limited by kinetic constraints due to the low electronic conductivity. Meanwhile, the higher I-Li content in the Ge anode reflects more pronounced interfacial side reactions between potential-plated Li and LPSCl, which are attributed to its significantly higher electronic conductivity relative to its ionic conductivity. Remarkably, the Si_7Ge anode shows the lowest QA-Li (6.1%) and I-Li (4.6%) among all samples, highlighting its improved kinetic reversibility and highly stable interphase during cycling.

To gain deeper insights into the interfacial reactions between the anode and the solid-state electrolyte during cycling, X-ray photoelectron spectroscopy (XPS) depth profiling was conducted. As shown in Figure 3g, the characteristic Li-Si peak located at 98.1 eV for the Si anode increases after etching, suggesting a higher concentration of trapped active Li. Concurrently, the peak at 100.8 eV, corresponding to $\text{Li}-\text{Si}-\text{PS}_4^{3-}$ species, evidences interfacial side reactions between the anode and the solid electrolyte^[29]. For the Ge anode, the surface is dominated by the Ge-S signal with a binding energy of 30.9 eV. After 5 min of etching, a Ge-Li signal at 27.6 eV becomes apparent (Figure 3h). These observations indicate that the relatively high electronic conductivity of the Ge anode, compared to its ionic conductivity, promotes localized lithium plating and facilitates the formation of an unstable interphase with the LPSCl electrolyte. As a sharp contrast, the Si_7Ge anode exhibits a peak at 28.5 eV, attributed to Ge-Ge/Si, which indicates that the balanced electronic/ionic transport effectively alleviates interfacial side reactions and reduces trapped active Li (Figure S26, Supporting Information). Besides, the Li-Si peak for the Si_7Ge anode is weak, indicating reduced residual active Li in Si_7Ge (Figure 3i). And the stable Li-Si-O peak at 101.9 eV for both pristine and etched anodes suggests the formation of a stable interphase. Analysis of the S 2p spectra reveals binding energies at 161.5 eV and 159.9 eV, corresponding to PS_4^{3-} in LPSCl and the decomposition product Li_2S , respectively^[29]. As shown in Figure 3j, the Li_2S content on the Si anode gradually increases from 13.0% to 14.6% after etching, while the Ge anode exhibits the highest Li_2S decomposition, from 18.1% to 18.9% (Figure 3k). For the Si_7Ge anode, less decomposed Li_2S is observed, with a content of 12.0% after etching (Figure 3l). These results suggest that the superior and well-balanced electronic and ionic conductivities of the Si_7Ge anode enable more efficient lithium extraction and facilitate the formation of a stable interphase.

Collectively, insufficient electronic transport in Si anodes results in trapped QA-Li within residual Li_xSi and impaired kinetics, leading to low ICE and poor rate performance (Figure 4a). Conversely, despite markedly improved electronic conductivity

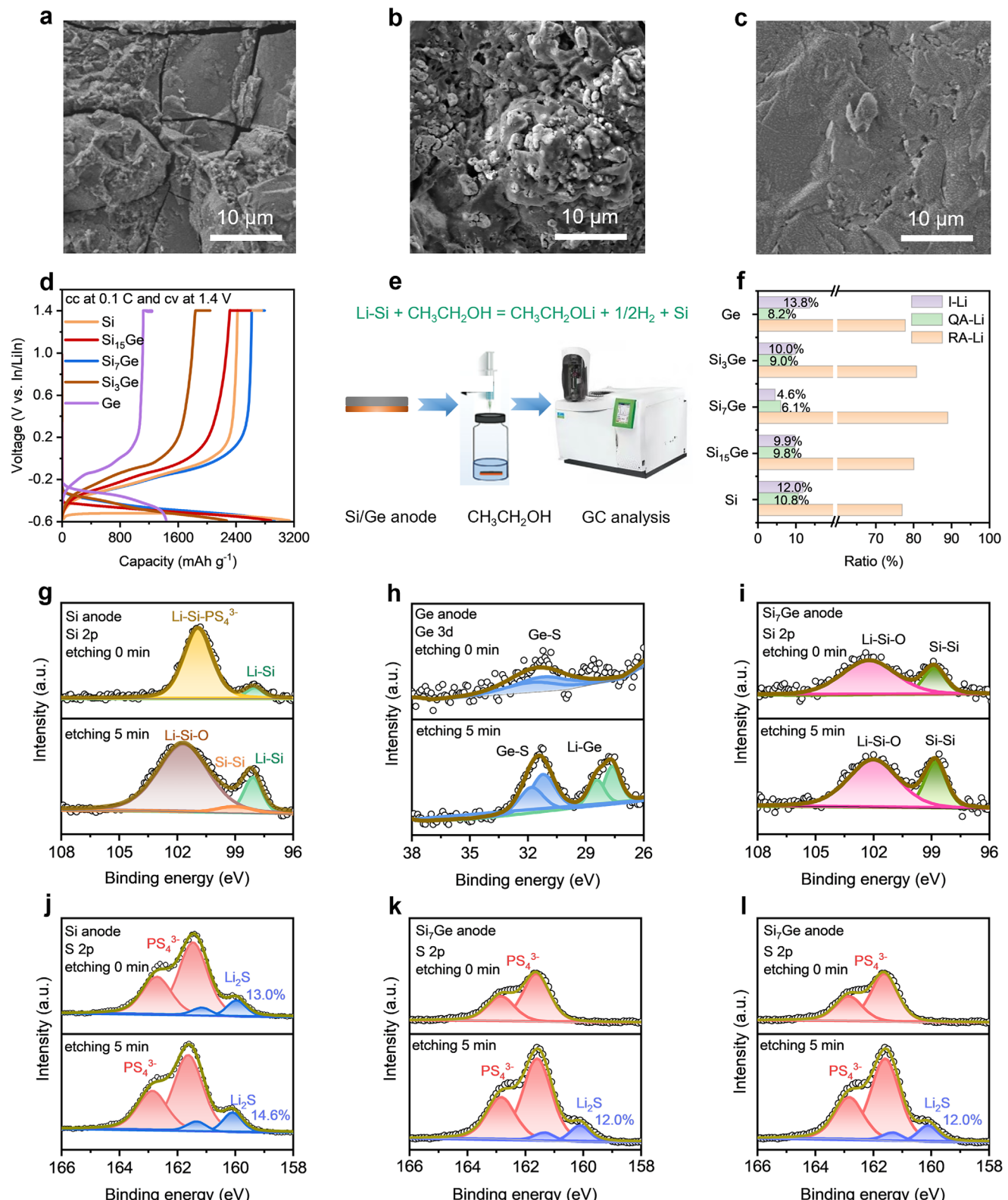


Figure 3. Structural evolution and analysis of various anodes. **a–c** Top-view SEM images of (a) Si anode, (b) Ge anode, and (c) Si_7Ge anode after 100 cycles. **d**) Charge processes under constant current at 0.1 C and consistent voltage at 1.4 V for various anodes. **e**) Schematic illustrating the procedure used to quantify inactive Li in various delithiated anodes. **f**) Ratio analysis of reversible active Li (RA-Li), quasi-reversible active Li (QA-Li), and inactive Li (I-Li) for various anodes. **g–l**) High-resolution XPS spectra: (g) Si 2p for Si anode, (h) Ge 3d for the Ge anode, (i) Si 2p for Si_7Ge anode, (j) S 2p for Si anode, (k) S 2p for Ge anode, and (l) S 2p for Si_7Ge anode.

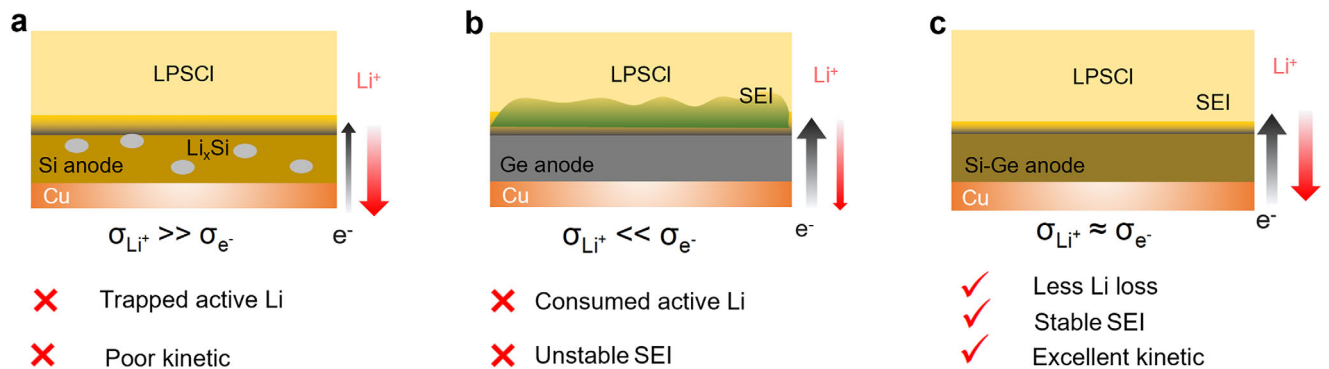


Figure 4. Schematic diagram illustrating electron transport and Li^+ migration behaviors in different anodes within ASSBs. a) The inherently poor electronic conductivity and limited Li^+ transport kinetics at the Si anode hinder the achievable capacity and rate capability in ASSBs. b) The inherently high electronic conductivity, combined with limited Li^+ transport kinetics at the Ge anode, leads to the formation of an unstable interphase and the consumption of active Li. c) The Si-Ge solid solution anode demonstrates improvements in both electronic conductivity and Li^+ diffusivity, achieving balanced electron and Li^+ transport, which effectively enhances the electrochemical performance in ASSBs.

in Ge anodes, restricted ionic transport facilitates Li plating and severe solid electrolyte side reactions, leading to an unstable interface and loss of active Li (Figure 4b). By comparison, the optimized Si₇Ge anode achieves a balanced and simultaneous improvement in both electronic and ionic conductivities, facilitating the formation of a stable interface and minimizing active lithium loss, thereby delivering superior kinetic performance (Figure 4c).

To further evaluate the practical viability of different anodes, full-cell configurations paired with HV-LCO and NCM cathode are systematically investigated (Figure S27, Supporting Information). Figure 5a presents the initial charge/discharge profiles of full cells assembled with different anodes and the HV-LCO cathode at 0.1 C. The initial charge voltage profiles reveal that the full cell with the Si anode exhibits the highest initial voltage,

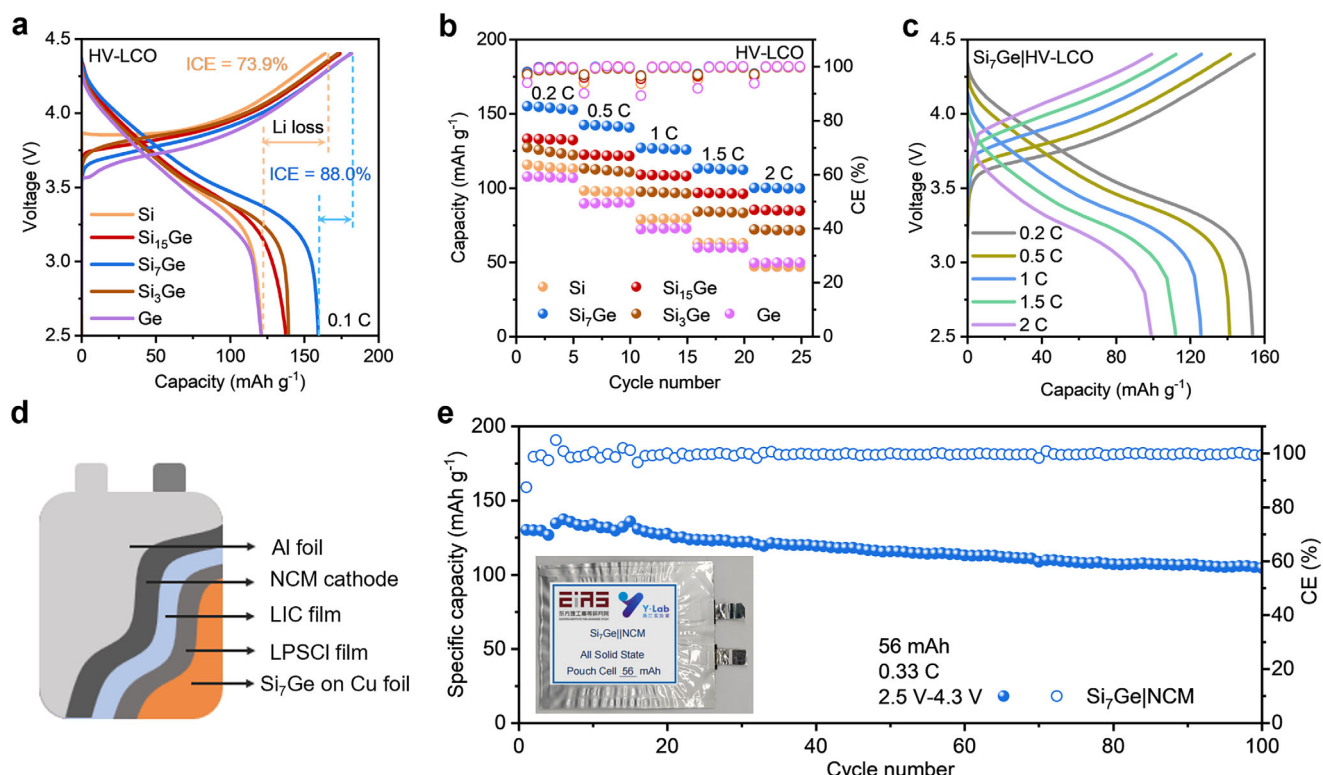


Figure 5. Full-cell electrochemical performance of Si-Ge solid solution in ASSBs. a) Galvanostatic charge and discharge profiles of various anodes coupled with the HV-LCO cathode during the first cycle. b) Rate performance of full cells with different anodes. c) Galvanostatic charge and discharge profiles of the full cell (Si₇Ge|HV-LCO) at different rates. d) Schematic diagram of the structure of a Si-based all-solid-state pouch cell. e) Long-term cycling performance of the Si₇Ge|NCM pouch cell.

which reflects low lithiation potential and large overpotential due to sluggish reaction kinetics. In contrast, the Ge anode shows a lower initial voltage, owing to its relatively higher lithiation potential, which narrows the potential gap with the cathode.^[5] The Si-Ge solid solution anodes display intermediate initial voltages that are lower than those of pure Si. This is attributed to the elevated lithiation potential and reduced overpotential enabled by Ge incorporation, leading to improved reaction kinetics and interfacial transport.^[35] The Si anode-based full cell delivers charge/discharge capacities of 165/122 mAh g⁻¹, with an ICE of 73.9%. Comparatively, the Ge anode-based full cell shows a lower charge plateau and serious interfacial side reactions, resulting in charge/discharge capacities of 183/122 mAh g⁻¹ and an ICE as low as 66.5%. Notably, the precisely modulated Si₇Ge anode exhibits superior performance, achieving charge/discharge capacities 182/160 mAh g⁻¹ and a record-high ICE of 88.0%, outperforming other alloys such as Si₁₅Ge and Si₃Ge anodes. Rate performance test (Figure 5b) reveals that the Si₇Ge-based full cell maintains high discharge capacities of 154, 142, 126, 113, and 100 mAh g⁻¹ at 0.2 C, 0.5 C, 1 C, 1.5 C, and 2 C, respectively, owing to its high RA-Li content and balanced ionic/electronic transport. The corresponding voltage profiles at various rates are shown in Figure 5c, indicating minimal polarization even at 2 C. The assembled Si₇Ge|HV-LCO full cell exhibits superior cycling stability compared to other counterparts, even after 100 cycles (Figure S28, Supporting Information). The Si₇Ge|HV-LCO full cell delivers a high discharge capacity of 136 mAh g⁻¹ at 0.5 C with a capacity retention of 83.8% after 100 cycles. Additionally, the Si₇Ge|HV-LCO full cell exhibits stable cycling performance over 200 cycles at 2 C, retaining 80% of its initial capacity (Figure S29, Supporting Information). Owing to the enhanced and balanced electronic and ionic conductivity of Si₇Ge, high-loading Si₇Ge anode achieves a high areal capacity of up to 10.2 mAh cm⁻² (Figure S30, Supporting Information). Figure 5d shows a schematic of the Si-based all-solid-state pouch cell structure, where wet-coated Si₇Ge on Cu foils are integrated with dry-processed electrolyte and NCM cathode films through lamination under static pressure. The resulting Si₇Ge|NCM all-solid-state pouch cell delivers a discharge capacity of 56.8 mAh at 0.1 C (Figure 5e, Figure S31, Supporting Information), and maintains a capacity 130 mAh g⁻¹ at 0.33 C over 100 cycles at 25°C (Figure S32, Supporting Information). These results demonstrate the practical applicability of additive-free Si-based alloy anodes in industrial-scale solid-state batteries.

3. Conclusion

In summary, a series of Si-Ge infinite solid solutions were successfully synthesized via high-energy ball milling and employed as high-performance anode materials for ASSBs. The isovalent substitution of Si with Ge, featuring a lower bandgap and larger atomic radius, simultaneously enhances the electronic and ionic conductivities of the host matrix. As a result, the optimized Si₇Ge anode with balanced electronic and ionic transport exhibits a high ICE of 89.4%, a high reversible capacity of 2631 mAh g⁻¹, and superior rate performance, maintaining 2024 mAh g⁻¹ at a high current density of 3 C. Furthermore, an all-solid-state pouch cell assembled with the Si₇Ge anode and LiNi_{0.88}Co_{0.09}Mn_{0.03}O₂ cathode demonstrates stable cycling performance over 100 cycles at

0.33 C, underscoring the practical viability of the material. Importantly, the obtained Si₇Ge exhibits intrinsically enhanced conductivity without the need for additional conductive additives or embedded solid-state electrolyte phases, thereby reducing interfacial complexities and parasitic reactions. This work offers a promising pathway to overcome the intrinsic limitations of Si-based anodes, paving the way for high-energy-density and durable ASSBs suitable for next-generation energy storage systems.

4. Experimental Section

Detailed experimental procedures can be found in the Supporting Information.

Supporting Information

Supporting Information is available from the Wiley Online Library or from the author.

Acknowledgements

Yaru Li, Shengjie Xia, and Guantai Hu are co-first authors. This work was supported by the Key R&D Program of Zhejiang (2024SSYS0050), the "Innovation Yongjiang 2035" Key R&D Program (2025Z063, 2024Z040), the National Natural Science Foundation of China (22409173, 22409103, W2441017), and the Zhejiang Provincial Natural Science Foundation of China (LQ24B030015). Prof. C. Wang also acknowledges the support of Eastern Institute of Technology, Ningbo, China.

Conflict of Interest

The authors declare no conflict of interest.

Data Availability Statement

The data that support the findings of this study are available from the corresponding author upon reasonable request.

Keywords

all-solid-state batteries, electronic conductivity, ionic conductivity, Si-Ge solid solutions, silicon anode

Received: June 15, 2025

Revised: July 24, 2025

Published online:

- [1] E. P. Alsac, D. L. Nelson, S. G. Yoon, K. A. Cavallaro, C. Wang, S. E. Sandoval, U. D. Eze, W. J. Jeong, M. T. McDowell, *Chem. Rev.* **2025**, 125, 2009.
- [2] J. Carey, *Proc. Natl. Acad. Sci. USA* **2024**, 121, 2425219121.
- [3] J. Zhang, J. Fu, P. Lu, G. Hu, S. Xia, S. Zhang, Z. Wang, Z. Zhou, W. Yan, W. Xia, C. Wang, X. Sun, *Adv. Mater.* **2024**, 37, 2413499.
- [4] J. A. Lewis, K. A. Cavallaro, Y. Liu, M. T. McDowell, *Joule* **2022**, 6, 1418.
- [5] W. J. Jeong, C. Wang, S. G. Yoon, Y. Liu, T. Chen, M. T. McDowell, *ACS Energy Lett.* **2024**, 9, 2554.

- [6] W. Li, M. Li, S. Wang, P.-H. Chien, J. Luo, J. Fu, X. Lin, G. King, R. Feng, J. Wang, J. Zhou, R. Li, J. Liu, Y. Mo, T.-K. Sham, X. Sun, *Nat. Nanotech.* **2025**, *20*, 265.
- [7] H. Huo, J. Janek, *ACS Energy Lett.* **2022**, *7*, 4005.
- [8] Z. Sun, Q. Yin, H. Chen, M. Li, S. Zhou, S. Wen, J. Pan, Q. Zheng, B. Jiang, H. Liu, K. Kim, J. Li, X. Han, Y. B. He, L. Zhang, M. Li, Q. Zhang, *Interdiscip. Mater.* **2023**, *2*, 635.
- [9] M. Li, D. Xue, Z. Rong, R. Fang, B. Wang, Y. Liang, X. Zhang, Q. Huang, Z. Wang, L. Zhu, L. Zhang, Y. Tang, S. Zhang, J. Huang, *Adv. Funct. Mater.* **2024**, *35*, 2415696.
- [10] M. Zhao, J. Zhang, C. M. Costa, S. Lanceros-Méndez, Q. Zhang, W. Wang, *Adv. Mater.* **2023**, *36*, 2308590.
- [11] S. Jun, G. Lee, Y. B. Song, H. Lim, K. H. Baeck, E. S. Lee, J. Y. Kim, D. W. Kim, J. H. Park, Y. S. Jung, *Small* **2024**, *20*, 2309437.
- [12] P. Zheng, J. Sun, H. Liu, R. Wang, C. Liu, Y. Zhao, J. Li, Y. Zheng, X. Rui, *Batteries Supercaps* **2022**, *6*, 202200481.
- [13] M. Bai, X. Tang, M. Zhang, H. Wang, Z. Wang, A. Shao, Y. Ma, *Nat. Commun.* **2024**, *15*, 5375.
- [14] B. Zhu, G. Liu, G. Lv, Y. Mu, Y. Zhao, Y. Wang, X. Li, P. Yao, Y. Deng, Y. Cui, J. Zhu, *Sci. Adv.* **2019**, *5*, aax0651.
- [15] J. Tao, J. Han, Y. Wu, Y. Yang, Y. Chen, J. Li, Z. Huang, Y. Lin, *Energy Storage Mater.* **2024**, *64*, 103082.
- [16] H. Murata, K. Nozawa, T. Suzuki, Y. Kado, T. Suemasu, K. Toko, *Sci. Rep.* **2022**, *12*, 13779.
- [17] D. Cao, T. Ji, A. Singh, S. Bak, Y. Du, X. Xiao, H. Xu, J. Zhu, H. Zhu, *Adv. Energy Mater.* **2023**, *13*, 2203969.
- [18] J. Kim, C. Kim, I. Jang, J. Park, J. Kim, U. Paik, T. Song, *J. Power Sources* **2021**, *510*, 230425.
- [19] J. Y. Kim, S. Jung, S. H. Kang, J. Park, M. J. Lee, D. Jin, D. O. Shin, Y. G. Lee, Y. M. Lee, *Adv. Energy Mater.* **2021**, *12*, 2103108.
- [20] D. Cao, X. Sun, Y. Li, A. Anderson, W. Lu, H. Zhu, *Adv. Mater.* **2022**, *34*, 2200401.
- [21] Y. Huang, B. Shao, Y. Wang, F. Han, *Energy Environ. Sci.* **2023**, *16*, 1569.
- [22] L. Cui, S. Zhang, J. Ju, T. Liu, Y. Zheng, J. Xu, Y. Wang, J. Li, J. Zhao, J. Ma, J. Wang, G. Xu, T.-S. Chan, Y.-C. Huang, S.-C. Haw, J.-M. Chen, Z. Hu, G. Cui, *Nat. Energy* **2024**, *9*, 1084.
- [23] H. Huo, M. Jiang, Y. Bai, S. Ahmed, K. Volz, H. Hartmann, A. Henss, C. V. Singh, D. Raabe, J. Janek, *Nat. Mater.* **2024**, *23*, 543.
- [24] D. H. S. Tan, Y.-T. Chen, H. Yang, W. Bao, B. Sreenarayanan, J.-M. Doux, W. Li, B. Lu, S.-Y. Ham, B. Sayahpour, J. Scharf, E. A. Wu, G. Deysher, H. E. Han, H. J. Hahn, H. Jeong, J. B. Lee, Z. Chen, Y. S. Meng, *Science* **2021**, *373*, 1494.
- [25] H. J. Shin, J. T. Kim, D. Han, H. S. Kim, K. Y. Chung, J. Mun, J. Kim, K. W. Nam, H. G. Jung, *Adv. Energy Mater.* **2024**, *15*, 2403247.
- [26] S.-Y. Ham, E. Sebti, A. Cronk, T. Pennebaker, G. Deysher, Y.-T. Chen, J. A. S. Oh, J. B. Lee, M. S. Song, P. Ridley, D. H. S. Tan, R. J. Clément, J. Jang, Y. S. Meng, *Nat. Commun.* **2024**, *15*, 2991.
- [27] Y. Ji, Z. Wang, C. Zhao, Z. Fang, Y. Gong, Q. Jing, Y. Xia, T. Luan, Y. Jiang, J. Liang, X. Li, M. Zhao, X. Zhai, X. Bie, T. Jiang, D. Geng, X. Sun, *Renewables* **2024**, *2*, 194.
- [28] S. Jing, Y. Lu, Y. Huang, H. Liu, Y. Shen, W. Kuang, H. Shen, S. Liu, Z. Zhang, F. Liu, *Adv. Mater.* **2024**, *36*, 2312305.
- [29] Z. Zhang, Z. Sun, X. Han, Y. Liu, S. Pei, Y. Li, L. Luo, P. Su, C. Lan, Z. Zhang, S. Xu, S. Guo, W. Huang, S. Chen, M.-S. Wang, *Energy Environ. Sci.* **2024**, *17*, 1061.
- [30] Z. Zhang, X. Zhang, Y. Liu, C. Lan, X. Han, S. Pei, L. Luo, P. Su, Z. Zhang, J. Liu, Z. Gong, C. Li, G. Lin, C. Li, W. Huang, M.-S. Wang, S. Chen, *Nat. Commun.* **2025**, *16*, 1013.
- [31] W. Yan, Z. Mu, Z. Wang, Y. Huang, D. Wu, P. Lu, J. Lu, J. Xu, Y. Wu, T. Ma, M. Yang, X. Zhu, Y. Xia, S. Shi, L. Chen, H. Li, F. Wu, *Nat. Energy* **2023**, *8*, 800.
- [32] Z. Wang, X. Shen, S. Chen, R. Qiao, B. Sun, J. Deng, J. Song, *Adv. Mater.* **2024**, *36*, 2405025.
- [33] C. Fang, J. Li, M. Zhang, Y. Zhang, F. Yang, J. Z. Lee, M. H. Lee, J. Alvarado, M. A. Schroeder, Y. Yang, B. Lu, N. Williams, M. Ceja, L. Yang, M. Cai, J. Gu, K. Xu, X. Wang, Y. S. Meng, *Nature* **2019**, *572*, 511.
- [34] E. Kaeli, Z. Jiang, X. Yang, E. P. K. L. Choy, N. B. Liang, E. Barks, S. Wang, S. D. Kang, W. C. Chueh, *Energy Environ. Sci.* **2025**, *18*, 1452.
- [35] Y. Chen, Y. Lakhdar, L. Chen, B. Kishore, J. Choi, E. Williams, D. Spathara, R. Jackowska, E. Kendrick, *Next Energy* **2024**, *5*, 100166.